ORIGINAL ARTICLE

Dynamic evaluation on ride comfort of metro vehicle considering structural flexibility

Zhaowei Chen[1] · Guo Zhu[1]

Abstract

Traditional rigid vehicle model cannot reflect structural local vibration and flexible deformation, which may affect the accuracy in evaluating ride comfort of metro vehicle. Aiming at this issue, this paper proposes a research method of flexible dynamic behavior based on flexible multi-body dynamics (FMBD), considering the structural flexibilities of key parts of metro vehicle in detail, to study the ride comfort of metro vehicle. First, finite element models of carbody and frame are established, which are then reduced by substructure theory and Guyan reduction method. On this basis, the flexible vehicle-track coupled dynamic model is established. After investigating the difference between the flexible model and traditional rigid model, the ride comfort of metro vehicle on straight line and curve line is then evaluated subjected to rail random irregularity, short-wave excitation and long-wave excitation, respectively. Finally, correlations of carbody vibrations at different locations are deeply investigated. Results show that carbody accelerations calculated by flexible model are larger than those obtained by rigid model. The sensitive frequency band of human is obviously reflected and calculated by flexible model, indicating that the ride comfort of metro vehicle can be more accurately evaluated with the flexible vehicle model. Flexible modes and local vibrations are obviously reflected in carbody vibrations. Vibration at PR (point on roof) location is largest, and vibration at PC (point on floor center) location is smallest. Ride comfort is very sensitive to long-wave excitation while is not sensitive to short-wave excitation. It is not accurate enough to evaluate ride comfort of metro vehicle only according to vibration at floor center, and more data at different locations should be concerned, especially vibrations at air spring locations.

Keywords Metro vehicle · Ride comfort · Flexible multi-body dynamics · Vehicle-track dynamics · Short-wave excitation · Long-wave excitation · Cross-correlation

1 Introduction

Multi-body dynamics (MBD) is one of the most important methods in the evaluation of dynamic performance of railway vehicle [1]. Adopting this method, carbody, bogie and wheelset are considered as rigid bodies, and suspension system is simulated by spring-damping element to realize the connection of each rigid body [2]. With the addition of the corresponding constraints, the dynamic model of railway vehicle is formed and finally calculated by numerical integration [3]. However, with the requirements of high-speed and lightweight, MBD is hardly to meet the computational

accuracy in some high-precision studies [4]. In this case, flexible multi-body dynamics (FMBD) emerges in response to requirement, which is mainly used to obtain more accurate dynamic characteristics of vehicle based on the connection of finite element theory and MBD [5].

Nowadays, with the lightweight requirement of metro vehicle, the components of carbody and frame become thinner and lighter, which directly aggravate local vibrations of carbody and frame, and also change the natural vibration properties. However, the traditional vehicle dynamic model based on MBD cannot reveal local vibrations due to the key parts are modelled as rigid bodies [6]. Hence, to accurately evaluate the ride comfort and running performance of metro vehicle, the vehicle should be modeled by FMBD.

At present, FMBD has been used by many scholars to study the dynamic characteristics of railway vehicles. It is observed that the resonant frequency is obviously different from that of the rigid structure considering structural

✉ Zhaowei Chen
 chenzhaowei@my.swjtu.edu.cn

[1] School of Mechanotronics and Vehicle Engineering, Chongqing Jiaotong University, No.66 Xuefu Rd., Nan'an Dist., Chongqing, China

flexibility, which deteriorates the riding comforts obviously [7]. Gerardin and Cardona provided the formulation of flexible vehicle system based on an exhaustive treatment of large rotations and finite element modelling [8]. Huang et al. investigated low-frequency carbody hunting problem of a high-speed passenger car emerged in the process of tests and service operations [9]. Shi and Wu proposed feasible solutions to avoid the resonance of flexible vibration caused by the hunting motion of bogie which is close to that of car body using FMBD and finite element method (FEM) [10]. Gong et al. proposed a dynamic vibration absorber which shows very good performance and robustness to suppress the resonant vibration of the flexible car body [11]. Claus and Schiehlen [12] predicted dynamic stresses of a truck frame for a high-speed train using a flexible vehicle model by the FEM-FMBD approach and found that the middle frequency motion cannot be neglected in the calculations of the dynamic bending stress distribution. And then the noise of car body excited by the polygonalised wheel is further studied by the same numerical procedure [13]. Calbom found that the modal selection plays a quite important role in the accuracy and numerical efficiency when the modal data are incorporated into the MBS dynamics code [14]. Saporito et al. proposed an experimental validation of the vehicle model with a flexible carbody and flexible truck frames, and considered the effect of the carbody flexibility on the L/V (Y/Q) ratio [15]. Existing references have proposed many significant models and conclusions, but most of them only considered the flexibility of carbody, while few works regarded frame as flexible body. It should be underlined that the flexible frame model can provide accurate suspension forces, which directly affects the carbody vibration and ride comfort. Hence, the flexibilities of carbody and frame should be both considered. Moreover, in the existing studies, the adopted line conditions and track excitations are simple, which are not effective enough to present the differences between rigid vehicle model and flexible vehicle model.

This paper presents a method to research ride comfort for metro vehicles based on FMBD. First, the methodology of dynamic evaluation on ride comfort of metro vehicle based on FMBD is presented. In the method, the carbody model and frame model are established by finite element theory, which are then reduced based on substructure theory [16] and Guyan reduction matrix method [17]. Based on the formulated model, the ride comfort of metro vehicle under different line conditions (including rail random irregularity, short-wave excitation and long-wave excitation) is studied. Moreover, a multi-rigid-body dynamic model of metro vehicle is established and compared with the flexible model to study the influence of structural flexibility on the ride comfort of metro vehicle. Finally, some interesting conclusions are reached in the end.

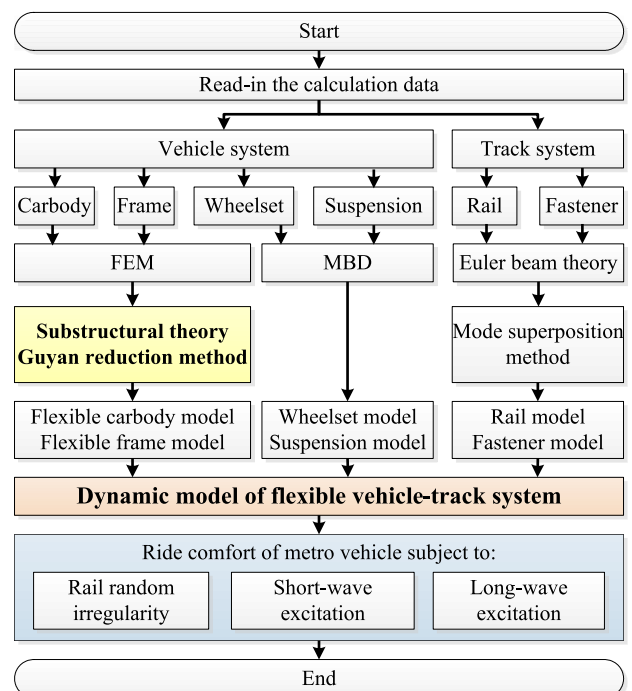# 2 Methodology of dynamic evaluation on ride comfort of metro vehicle based on flexible multi-body dynamics

The methodology of dynamic evaluation on ride comfort of metro vehicle based on FMBD is shown in Fig. 1. As can be seen from the figure, the models of key parts of the vehicle are established through finite element theory primarily [18]. Then, the finite element equations are reduced by the substructure theory to reduce the computational equations. Finally, the metro vehicle dynamics model is formed. The detailed methodology is presented below in this section.

It should be noted that, carbody and frame are considered as flexible bodies in this work, while wheelset is regarded as rigid body due to the elastic deformation of wheelset is relatively small, which has almost no influences on ride comfort of vehicle [19].

2.1 Vehicle submodel

The vehicle consists of several key parts, including the carbody, the frame, the wheelset and the suspension (Fig. 2). The detailed modelling information of these parts are presented below.

1. Carbody

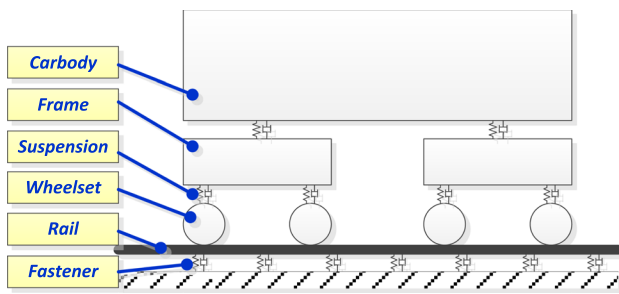**Fig. 1** Methodology of dynamic evaluation on ride comfort of metro vehicle based on FMBD

Fig. 2 Flexible vehicle-track model
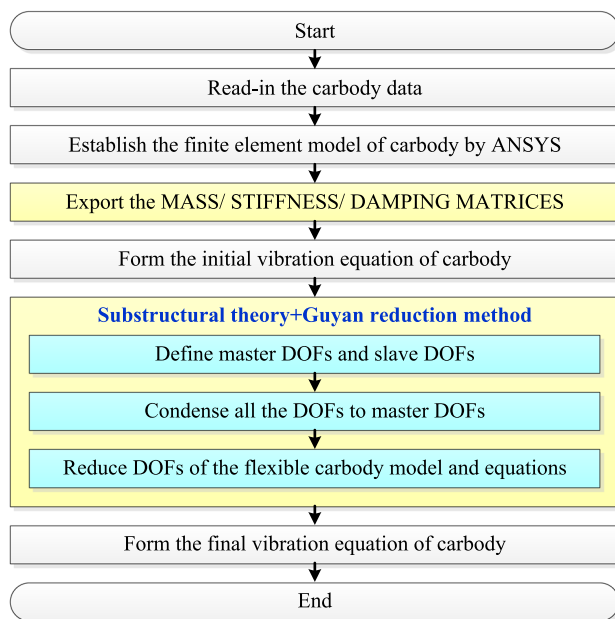

Fig. 3 Modelling process of flexible carbody

Fig. 4 Secondary suspension force with the change of element size

Fig. 5 Finite element model of carbody

The carbody is modelled as flexible body, and the modelling process is presented in Fig. 3. As seen from Fig. 3, the finite element model should be established primarily to export the mass/stiffness/damping matrices. The finite element model of carbody is built by ANSYS with the element SHELL 63.

In the simulation of carbody in ANSYS, the size of element is a key parameter to ensure the calculation accuracy. The computational efficiency drops sharply if the size is too small; while the calculation error increases if size is too large. Hence, a pre-calculation is conducted to determine the size of element adopted in the following studies, as seen in Fig. 4.

In this pre-calculation, the rail irregularity is not considered, and the parameters of the vehicle-track system can be seen in the following Sect. 3.2. It should be noted that secondary suspension is installed between carbody
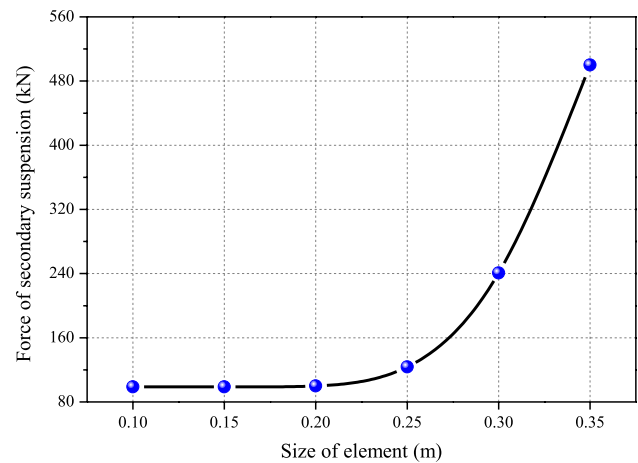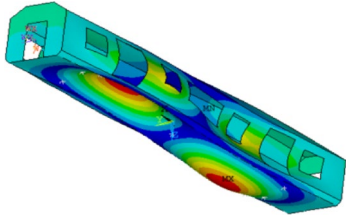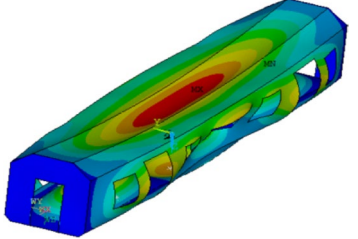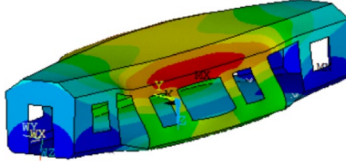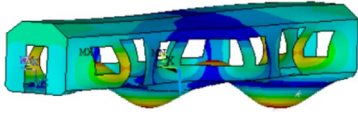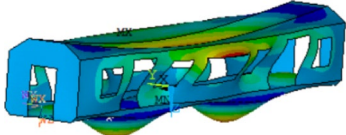
and bogie, which is the only device to transmit excitation between carbody and bogie, indicating that the suspension force greatly affects the vibration of carbody. Hence, the suspension force is adopted in this work to determine the proper element size of the carbody model in the pre-calculation. As seen from the results, the secondary suspension force is divergent (increase sharply) with the increase of the element size. Considering the calculation accuracy and efficiency, the element size for modelling carbody is 0.2 m.

Adopting the optimal element size, the finite element model of carbody is established, as seen in Fig. 5. The carbody model contains 18,168 nodes, 17,734 elements and 109,008 DOFs, whose natural properties are given in Table 1.

Table 1 Natural properties of carbody (First 6 modes)

Order	Vibration mode	Order	Vibration mode
1	5.03 Hz	2	6.11 Hz
3	6.33 Hz	4	7.40 Hz
5	8.00 Hz	6	8.84 Hz

Then, the mass/stiffness/damping matrices of the carbody can be exported and then form the vibration mode of carbody, as below:

$$M_c \ddot{u}_c + C_c \dot{u}_c + K_c u_c = F_c, \tag{1}$$

where u is the displacement vector, M is the mass matrix, C is the damping matrix, K is the stiffness matrix, F is the load vector, and subscript c represents the carbody.

It should be stated that Rayleigh damping [20] is adopted as the damping model in this work, thus the damping matrix C_c in Eq. (1) can be further expressed by

$$C_c = \alpha M_c + \beta K_c \tag{2}$$

$$\alpha = 2\omega_1\omega_2 \frac{(\xi_2\omega_1 - \xi_1\omega_2)}{\omega_1^2 - \omega_2^2} \tag{3}$$

$$\beta = 2 \frac{(\xi_1\omega_1 - \xi_2\omega_2)}{\omega_1^2 - \omega_2^2}, \tag{4}$$

where ω_1 and ω_2 are the natural vibration frequencies of first and second modes of carbody; ξ_1 and ξ_2 are the relevant damping ratios.

Because the carbody finite element model contains 109,008 DOFs, tremendous calculations should be conducted to solve the Eq. (1), which is hard to be performed on personal computer. On this basis, the substructure theory and Guyan reduction method are adopted to reduce the calculation equations of carbody model.

According to the reduction method (Fig. 3), all the DOFs of the carbody is divided into two parts, namely the master DOFs and the slave DOFs, which are expressed as $u_{c\alpha}$ and $u_{c\beta}$, respectively. Then, the relationship between $u_{c\alpha}$ and $u_{c\beta}$ is as follows:

$$u_{c\beta} = T u_{c\alpha}, \tag{5}$$

where T is the transformation matrix from the master DOFs to the slave DOFs.

Assuming that m master DOFs are selected from the carbody model, and n slave DOFs are left in the rest. $u_{c\alpha}$ and $u_{c\beta}$ are vectors of order m and order s, respectively, then the solution u_c can be expressed as:

$$u_c = \begin{bmatrix} u_{c\alpha} \\ u_{c\beta} \end{bmatrix} = \begin{bmatrix} E \\ T \end{bmatrix} u_{c\alpha} = \overline{T} u_{c\alpha}. \tag{6}$$

Since all the elements with external loads are selected as the master DOFs, external loads on the slave DOFs

are zero, then the flexible dynamic equations of the master DOFs of carbody can be obtained:

$$M_{c\alpha}\ddot{u}_{c\alpha} + C_{c\alpha}\dot{u}_{c\alpha} + K_{c\alpha}u_{c\alpha} = F_{c\alpha}. \tag{7}$$

It should be noted that some errors exist in the above equations, because these equations are obtained in static state. The errors can be eliminated when the following conditions are matched.

Equation (1) is converted into the following form:

$$\begin{bmatrix} M_{mm} & M_{ms} \\ M_{sm} & M_{ss} \end{bmatrix} \begin{Bmatrix} \ddot{u}_{c\alpha} \\ \ddot{u}_{c\beta} \end{Bmatrix} + \begin{bmatrix} C_{mm} & C_{ms} \\ C_{sm} & C_{ss} \end{bmatrix} \begin{Bmatrix} \dot{u}_{c\alpha} \\ \dot{u}_{c\beta} \end{Bmatrix} \\ + \begin{bmatrix} K_{mm} & K_{ms} \\ K_{sm} & K_{ss} \end{bmatrix} \begin{Bmatrix} u_{c\alpha} \\ u_{c\beta} \end{Bmatrix} = \begin{Bmatrix} F_{c\alpha} \\ 0 \end{Bmatrix}. \tag{8}$$

The error can be obtained as follows:

$$\Delta = -K_{ss}^{-1}\big[(M_{sm} - M_{ss}K_{ss}^{-1}K_{sm})\ddot{u}_{c\alpha} \\ + (C_{sm} - C_{ss}K_{ss}^{-1}K_{sm})\dot{u}_{c\alpha} \big]. \tag{9}$$

To eliminate the error, Δ should equal 0, then:

$$M_{sm} = M_{ss}K_{ss}^{-1}K_{sm} \tag{10}$$

$$C_{sm} = C_{ss}K_{ss}^{-1}K_{sm}. \tag{11}$$

Hence, the selection of master DOFs directly determines the validities of Eqs. (10) and (11).

Overall, the equations of flexible carbody after reduction is given in Eqs. (7), (10) and (11) are conditions to eliminate the error.

2. Other components

The flexible frame model can also be established based on the above method, which is not described in detail below. The reduced flexible frame equation is

$$M_{f\alpha}\ddot{u}_{f\alpha} + C_{f\alpha}\dot{u}_{f\alpha} + K_{f\alpha}u_{f\alpha} = F_{f\alpha}, \tag{12}$$

where subscript f represents frame, and subscript α denotes master DOFs.

Wheelset and suspension are modelled by traditional method, which can be referred to published reference [21].

2.2 Track submodel

The rails are modeled as Euler beams, and discretely supported by fasteners which are simulated as linear spring-damping elements. Three DOFs of each rail are taken into account, describing vertical motion, lateral motion and

torsional motion, and the equations of motion of the rail are given as

Vertical motion:

$$EI_y \frac{\partial^4 z_r(x,t)}{\partial x^4} + m_r \frac{\partial^2 z_r(x,t)}{\partial t^2} \\ = -\sum_{i=1}^{N_s} F_{rVi}(t)\delta(x - x_i) + \sum_{j=1}^{N_w} P_j(t)\delta(x - x_{wi}). \tag{13}$$

Lateral motion:

$$EI_z \frac{\partial^4 y_r(x,t)}{\partial x^4} + m_r \frac{\partial^2 y_r(x,t)}{\partial t^2} \\ = -\sum_{i=1}^{N_s} F_{rLi}(t)\delta(x - x_i) + \sum_{j=1}^{N_w} Q_j(t)\delta(x - x_{wi}). \tag{14}$$

Torsional motion:

$$GJ_t \frac{\partial^2 \phi_r(x,t)}{\partial x^2} + \rho_r I_{r0} \frac{\partial^2 \phi_r(x,t)}{\partial t^2} \\ = -\sum_{i=1}^{N_s} M_{Fi}(t)\delta(x - x_i) + \sum_{j=1}^{N_w} M_{wj}(t)\delta(x - x_{wi}). \tag{15}$$

In Eqs. (24)–(26), $z_r(x,t)$, $y_r(x,t)$, and $\phi_r(x,t)$ are vertical, lateral and torsional displacements of the rail, respectively; m_r is the rail mass per unit length; ρ_r is the rail density; EI_y and EI_z are the rail bending stiffness to Y-axle and Z-axle, respectively; I_{r0} is the torsional inertia of the rail; GJ_t is the rail torsional stiffness; $F_{rVi}(t)$ and $F_{rLi}(t)$ are the vertical and lateral dynamic forces of the ith fastener; $P_j(t)$ and $Q_j(t)$ are the jth wheel–rail vertical and lateral forces; $M_{Fi}(t)$ and $M_{wj}(t)$ are the moments applying on the rails due to forces $F_{rVi}(t)$ and $F_{rLi}(t)$ and due to forces $P_j(t)$ and $Q_j(t)$, respectively; x_i and x_{wj} are the locations of ith fastener and jth wheelset; N_s and N_w are the numbers of fasteners and wheelsets; and $\delta(x)$ is the Dirac delta function.

Then, the rail displacement can be finally described as

$$\begin{cases} z_r(x,t) = \sum_{k=1}^{N_z} Z_k(x)q_{zk}(t) \\ y_r(x,t) = \sum_{k=1}^{N_Y} Y_k(x)q_{yk}(t) \\ \phi_r(x,t) = \sum_{k=1}^{N_T} \phi_k(x)q_{tk}(t) \end{cases} \tag{16}$$

where, $Z_k(x)$, $Y_k(x)$ and $\Phi_k(x)$ are the rail vertical, lateral and torsional mode functions; $q_{zk}(t)$, $q_{yk}(t)$ and $q_{tk}(t)$ are the kth vertical, lateral and torsional mode time coordinates, respectively; and N_Z, N_Y and N_T are the total mode numbers of the rail vertical, lateral and torsional mode functions selected for the calculation.

2.3 Wheel–rail interaction

The nonlinear Hertzian elastic contact theory is used to calculate the wheel–rail normal contact forces:

$$P_N(t) = \left[\frac{1}{G}\delta N(t)\right]^{3/2}, \tag{17}$$

where G is the wheel–rail contact constant; $\delta N(t)$ is the wheel–rail normal elastic compression deformation.

Based on the Kalker's linear creep theory, the wheel–rail longitudinal creep force F_x, the lateral creep force F_y, and the spin creep torque M_z can be described by

$$\begin{cases} F_x = -f_{11}\xi_x \\ F_y = -f_{22}\xi_y - f_{23}\xi_{sp}, \\ M_z = f_{23}\xi_y - f_{33}\xi_{sp} \end{cases} \tag{18}$$

where f_{ij} represents the creep coefficients, and the definitions of the longitudinal, lateral and spin creepage ξ_x, ξ_y and ξ_{sp} are as follows:

$$\begin{cases} \xi_x = \frac{V_{w1}-V_{r1}}{V} \\ \xi_y = \frac{V_{w2}-V_{r2}}{V} \\ \xi_{sp} = \frac{\Omega_{w3}-\Omega_{r3}}{V} \end{cases} \tag{19}$$

in which V_{w1}, V_{w2} and Ω_{w3} are the longitudinal, lateral and spin speeds of the wheel at contact point, respectively; V_{r1}, V_{r2} and Ω_{r3} are the speeds of the rail at the contact point; and V is the wheelset speed moving on rails.

Since the Kalker's linear creep theory is only suited to the cases with small creepages, the non-linear modification should be made, for example, by Shen–Hedrick–Elkins model, for the situations of large creepages.

The wheel–rail interaction forces mainly include wheel–rail normal contact forces derived by nonlinear Hertzian elastic contact theory according to the elastic compression deformation of wheels and rails at contact points in the normal directions, and tangential wheel–rail creep forces, which are calculated first by Kalker's linear creep theory and then modified with the Shen–Hedrick–Elkins nonlinear model.

2.4 Vehicle–track coupled model

Based on the above submodels and equations, the metro vehicle-track coupled model is finally obtained as follows:

$$M\ddot{u} + C\dot{u} + Ku = F, \tag{20}$$

where u is the displacement matrix, M is the mass matrix, C is the damping matrix, K is the stiffness matrix, and F is the load matrix.

2.5 Numerical solution

To calculate the equation of the whole metro vehicle–track model, Zhai method [2], which is an explicit two-step numerical integration, is adopted:

$$\begin{cases} X_{n+1} = X_n + \dot{X}_n\Delta t + (0.5 + \psi)\ddot{X}_n\Delta t^2 - \psi\ddot{X}_{n-1}\Delta t^2 \\ \dot{X}_{n+1} = \dot{X}_n + (1 + \varphi)\ddot{X}_n\Delta t - \varphi\ddot{X}_{n-1}\Delta t \end{cases}, \tag{21}$$

where Δt is the time integral step, the subscript indicates which integral step the calculation is currently in, ψ and φ are independent parameters that control the characteristics of the integral method.

3 Comparison between flexible vehicle model and traditional rigid vehicle model

Before evaluating the ride comfort of metro vehicle, the differences between the established flexible vehicle model and traditional rigid vehicle model are investigated.

As an illustration, Figs. 6, 7 show carbody accelerations at PC (point on floor center) location, respectively, obtained by the established flexible vehicle model and traditional rigid vehicle model. In the simulation, the parameters of the vehicle can be found in the next section.

As seen from the comparisons, when the metro vehicle runs on the straight track, the carbody vertical acceleration obtained by the flexible vehicle model is obviously larger than that calculated by rigid model, especially in the frequency band of 4–10 Hz. It should be noted that, human is sensitive to the vertical vibrations in the frequency band of 4–8 Hz [22], indicating that the ride comfort of metro vehicle can be more accurately evaluated with the flexible vehicle model.

For lateral vibrations, the carbody lateral acceleration by flexible model is a little larger than that obtained by rigid model, especially under 1 Hz. According to reference [23], human is sensitive to the lateral vibrations below 2 Hz, also indicating that the flexible vehicle model is more accurate in studying ride comfort of metro vehicle.

Moreover, the Sperling index and RMS (root mean square) index, which are commonly employed in evaluating ride comfort, are listed in Table 2. As seen from the table, the ride comfort indices calculated by flexible model is larger than those obtained by rigid model due to the results by flexible model contain local vibrations and global flexible vibrations.

The differences between the flexible model and rigid model are obvious, hence it is suggested to employed flexible model in evaluating ride comfort of vehicle.
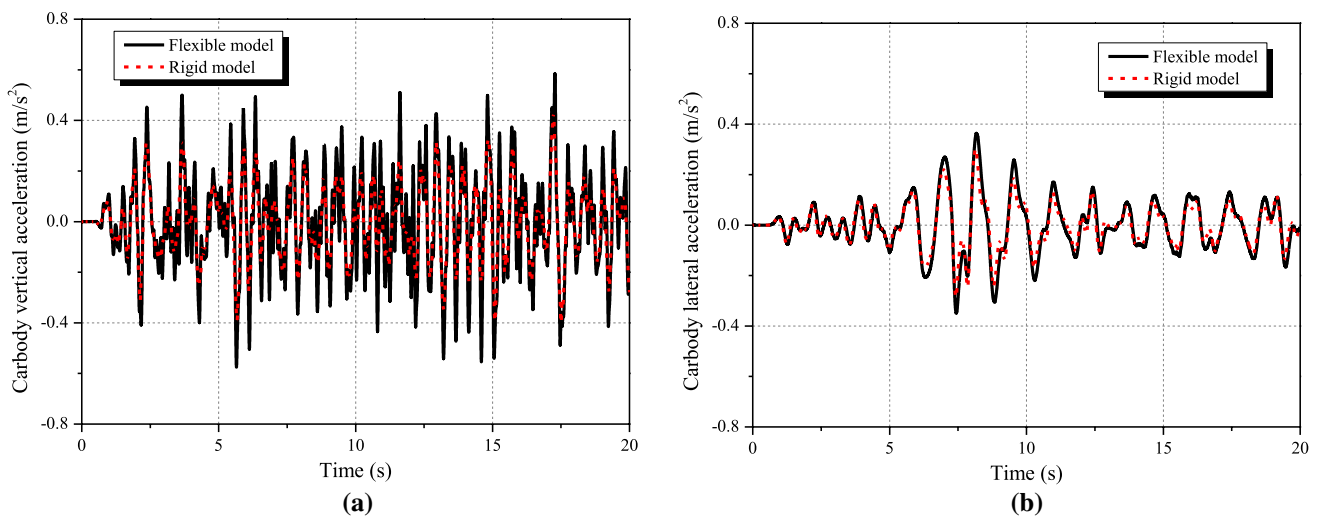
Fig. 6 Comparison of carbody accelerations in time domain: **a** Vertical acceleration, and **b** Lateral acceleration
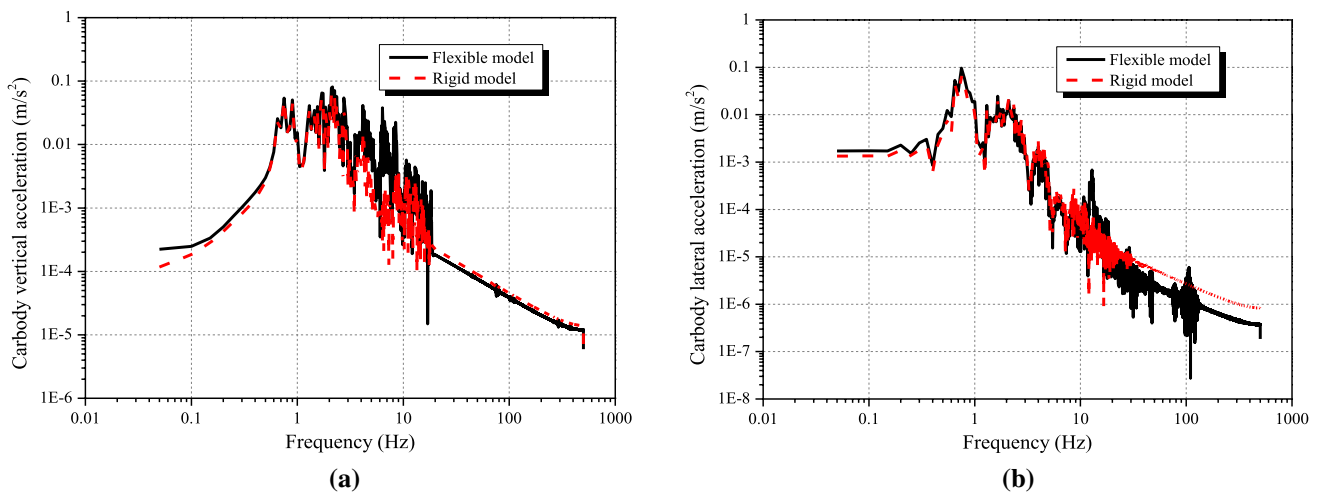

Fig. 7 Comparison of carbody accelerations in frequency domain: **a** Vertical acceleration, and **b** Lateral acceleration

Table 2 Comparison of Sperling index and RMS index

Item	Flexible model	Rigid model	Difference (×100%)
Vertical Sperling index	1.76	1.71	3.5%
Vertical RMS index	1.77	1.69	6.5%
Lateral Sperling index	1.46	1.45	4.1%
Lateral RMS index	1.63	1.62	4.3%

4 Evaluation conditions and parameters adopted in calculation

The evaluation conditions and parameters are introduced in detail in this part. Different line conditions and different track irregularities, including the rail random irregularity, short-wave excitation and long-wave excitation, are selected to conduct the following studies. The specific evaluation conditions are shown in Table 3.

In the evaluation conditions:

a. Curve line: the radius is 800 m, the length of transition curve is 55 m, and the superelevation is 0.095 m;

b. Rail random irregularity: The German high disturbance track irregularity is adopted;

c. Short-wave excitation: continuous sinusoidal excitation with a wavelength of 0.5 mm and a depth of 1 mm is used to simulate corrugation excitation;

d. Long-wave excitation: a single cosine excitation with a wavelength of 20 m and a depth of 10 cm is used to simulate settlement excitation;

Table 3 Evaluation conditions

Number of condition	Excitation	Line condition	Operating speed (km/h)
1–4	Rail random irregularity	Straight	50, 60, 70, 80
5–8	Rail random irregularity	Curve	50, 60, 70, 80
9–12	Short-wave excitation	Straight	50, 60, 70, 80
13–16	Long-wave excitation	Straight	50, 60, 70, 80

Table 4 Key parameters of metro vehicle

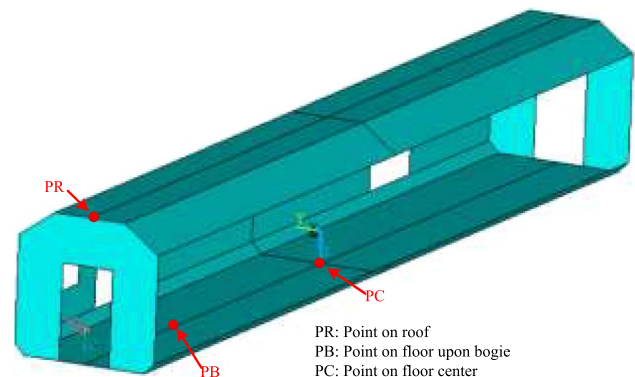| Parameter	Value
Mass of wheelset	1.878 t
Mass of frame	4.007 t
Total mass of carbody (including mass of passengers)	35.443 t
Moments of inertia of wheelset around the $x/y/z$ directions	1.055/0.139/1.055 t·m^2
Moments of inertia of frame around the $x/y/z$ directions	1.194/0.876/2.099 t·m^2
Moments of inertia of carbody around the $x/y/z$ directions	50.929/1410.96/1401.49 t·m^2
Stiffness of the primary suspension in the $x/y/z$ directions	7/4/0.9 MN/m
Damping of the primary suspension in the $x/y/z$ directions	10/10/10 kNs/m
Stiffness of the secondary suspension in the $x/y/z$ directions	220.1/220.1/341.9 kN/m
Damping of the secondary suspension in the $x/y/z$ directions	60/60/80 kNs/m

Table 5 Key parameters of track

Parameters	Value
Area of rail	7.745×10^{-3} m^2
Elasticity modulus of rail	2.1×10^5 MPa
Moments of inertia of rail	3.214×10^{-5} m^4
Fastener spacing	0.6 m
Stiffness of fastener	30 MN/m
Damping of fastener	10 kNs/m

PR: Point on roof
PB: Point on floor upon bogie
PC: Point on floor center

Fig. 8 Concerned locations on carbody

e. Key parameters of running metro vehicle and track are listed in Tables 4 and 5.

Carbody acceleration and Sperling index are adopted to evaluate the ride comfort of metro vehicle. The carbody accelerations of three locations are concerned in evaluation, as seen in Fig. 8, namely point on roof (PR), point on floor upon bogie (PB), and point on floor center (PC).

5 Evaluation on ride comfort of metro vehicle subject to rail random irregularity

Adopting the above model and parameters, the ride comfort of metro vehicle subject to rail random irregularity is evaluated in this part.

5.1 On straight segment

Taking the result at 80 km/h as an example to explain the ride comfort of vehicle in detail, Fig. 9 illustrates the acceleration of carbody. As seen from this figure, the vertical accelerations of PR and PB are almost the same, which are much larger than the vertical vibration of PC. This indicates that the vibration of floor center is relatively small, which is not suggested to be employed to accurately reveal carbody vibration and ride comfort. Due to the consideration of structural flexibility, the local vibrations and global bending/breathing/torsion vibrations are aroused, which directly lead to great vibrations at PR location and PB location. While for lateral vibrations, the vibration at

PR location is a little larger than that at PB location, and the vibration at PC location is much smaller.

Due to the local vibrations are aroused by the consideration of structural flexibility, the results in frequency domain should be investigated deeply. Figure 10 shows the carbody vertical acceleration at PR location in frequency domain. As seen from the figure, five peak frequencies are found:

1. Around 1 Hz. The frequencies are caused by rigid properties of carbody, which exist in both rigid vehicle model and flexible vehicle model;
2. 6.3 Hz. This is the coupled mode of the first-order vertical bending mode of roof and the third-order vertical bending mode of floor;

3. Around 8 Hz. This is the coupled mode of the second-order vertical bending mode of roof and the fourth-order vertical bending mode of floor;
4. Around 17.6 Hz. This is caused by the bending mode of roof and breathing mode of side walls;
5. 89.2 Hz. This is the vertical bending mode of roof at high frequencies.

It can be seen from the above explanations, all these modes contain vibrations of roof, which collectively form the vibration of PR.

Then, Fig. 11 shows the carbody vertical accelerations at all the concerned locations in frequency domain. As seen from the result, the frequencies are similar at difference locations, indicating that the vertical vibrations of carbody are mainly formed by these five frequency bands.
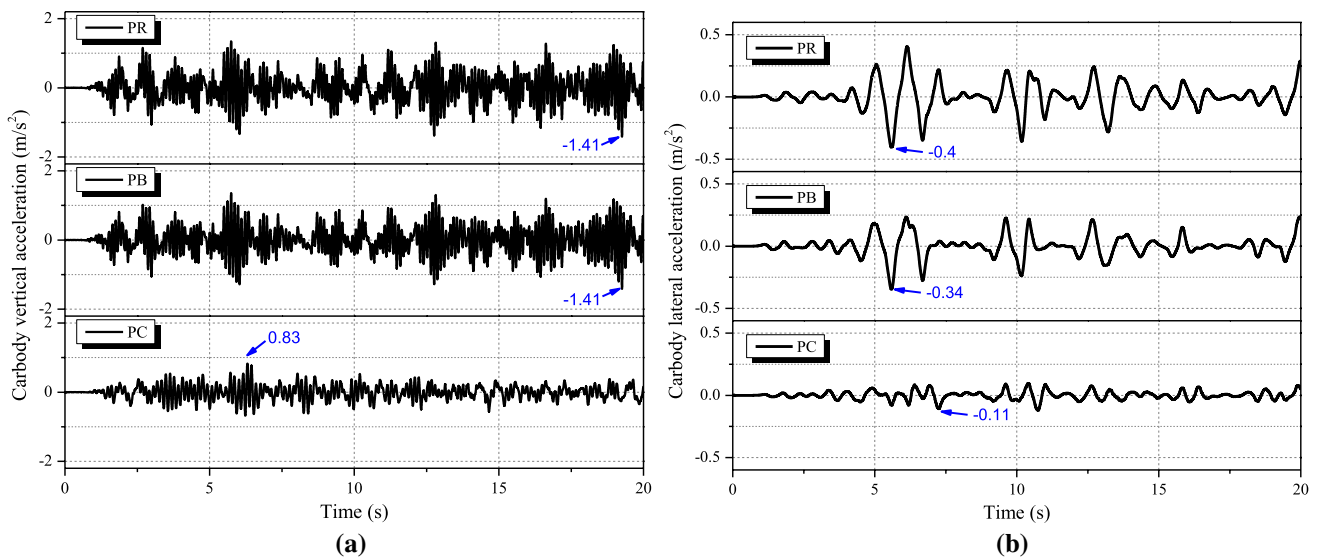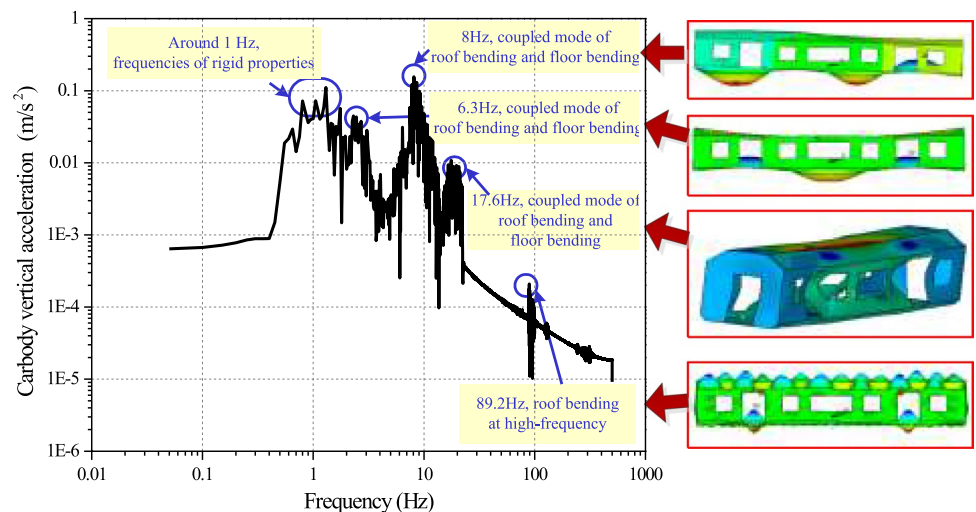
Fig. 9 Carbody acceleration ($v = 80$ km/h): **a** Vertical acceleration, and **b** Lateral acceleration

Fig. 10 Carbody vertical acceleration at PR location in frequency domain ($v = 80$ km/h)
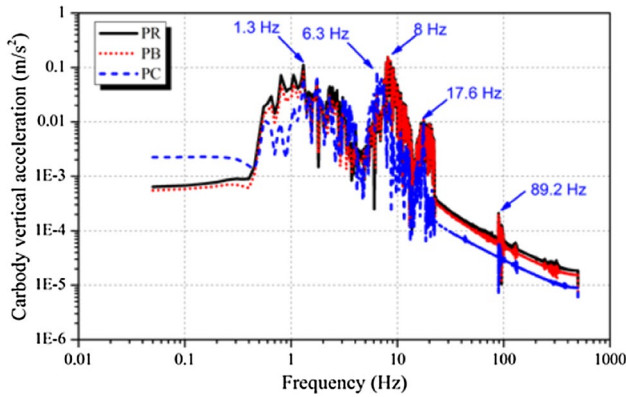
Fig. 11 Carbody vertical accelerations at all the concerned locations in frequency domain ($v=80$ km/h)
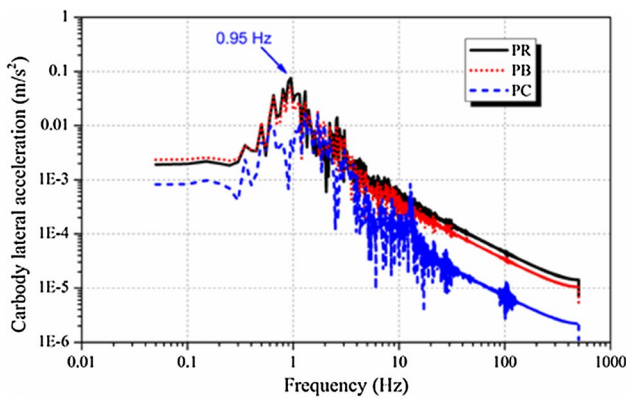

Fig. 12 Carbody lateral acceleration at all the concerned locations in frequency domain ($v=80$ km/h)

Moreover, the carbody lateral accelerations at different locations in frequency domain are given in Fig. 12. As seen from the result, the main frequency is 0.95 Hz, which is the frequency of rigid property of carbody. While other frequencies are not obviously aroused, indicating that the lateral vibrations of carbody are mainly formed by the vibration of side-walls, and the roof vibration and floor vibration have almost no influence on carbody lateral vibration. This similar conclusion can also be obtained from Table 1.

Furthermore, the peak values of carbody accelerations at PR location at different speeds are shown in Fig. 13. As seen from figures, the max acceleration increases with the increase of running speed. For vertical vibration, the acceleration at PR location are almost equal to that at PB location, which are larger than that at PC location. While for lateral vibration, the acceleration at PR location is the largest, and that at PC location is also the smallest.

The Sperling indices at different speeds are illustrated in Fig. 14. As seen from the result, with the increase of running speed, lateral and vertical Sperling indices increase. The vertical Sperling indices is larger than the lateral Sperling indices. All the calculated results are less than the ruled value in relevant code.

5.2 On curve segment

The result at 80 km/h are chosen to explain the ride comfort of vehicle on curve segment in detail, as seen in Fig. 15. As seen from the results, the vertical vibration of PR is almost the same with that of PB, which are
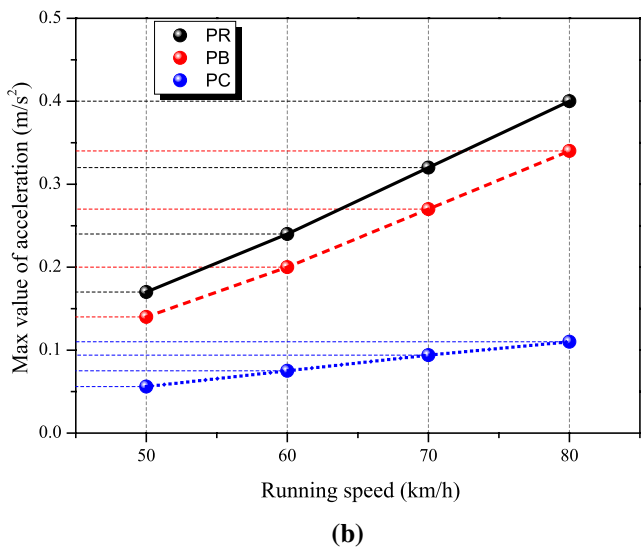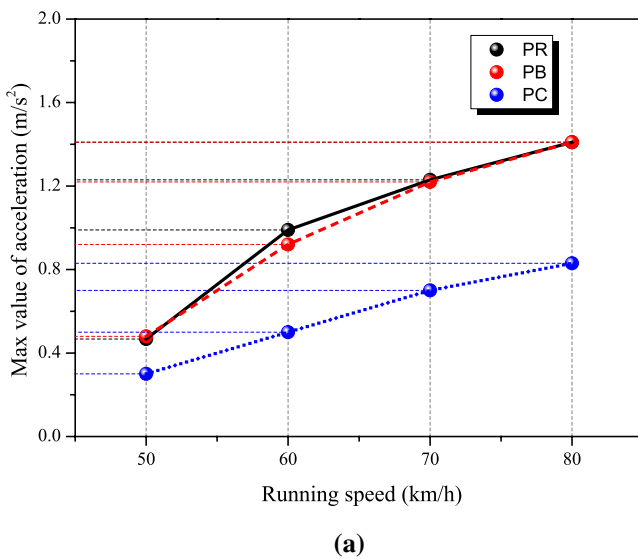

(a)

(b)

Fig. 13 Peak accelerations at different locations at different speeds
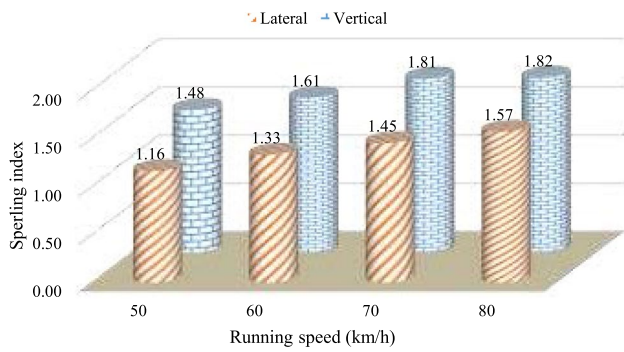
Fig. 14 Sperling index on straight segment

obviously larger than that of PC. While for lateral vibration, the acceleration at PR location is the largest, and that at PC location is the smallest.

To deeply investigate the carbody acceleration, Fig. 16 gives the results in frequency domain. The results of vertical acceleration in frequency domain are almost the same with those on straight segment, indicating that the vertical vibration of carbody is mainly formed by the vibrations in the five frequency bands. While for lateral acceleration, there is no obvious dominant frequency, indicating that the carbody lateral acceleration is mainly reflected by vibrations of sidewalls, and the roof vibration and floor vibration have only a little influence.

Furthermore, the Sperling index is given in Fig. 17. As seen from the result, with the increase of running speed, lateral and vertical Sperling indices increase. The vertical Sperling indices are larger than the lateral Sperling indices. All the calculated results are less than the ruled value in relevant code.
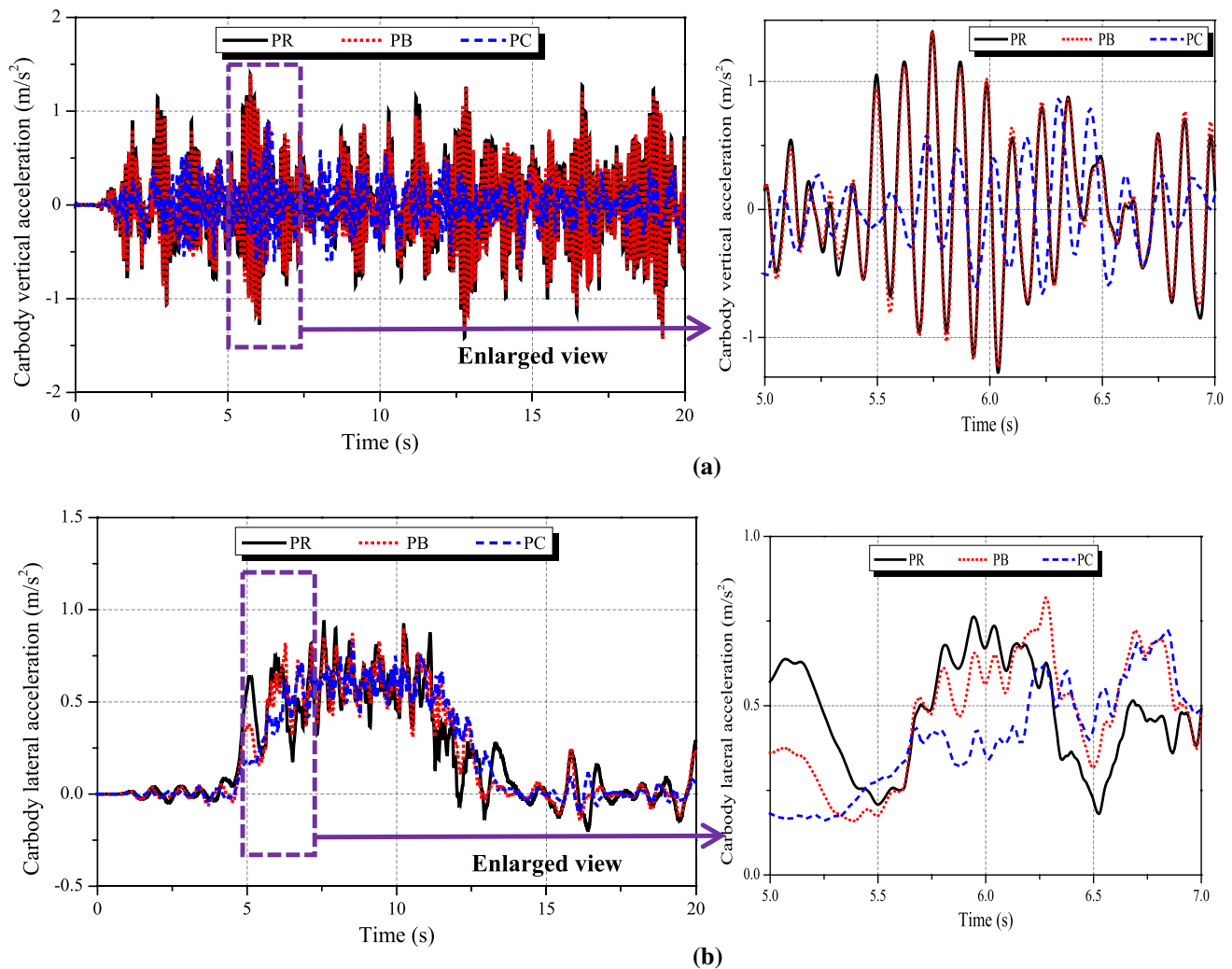

Fig. 15 Carbody acceleration on curve segment ($v = 80$ km/h): **a** Vertical acceleration, and **b** Lateral acceleration
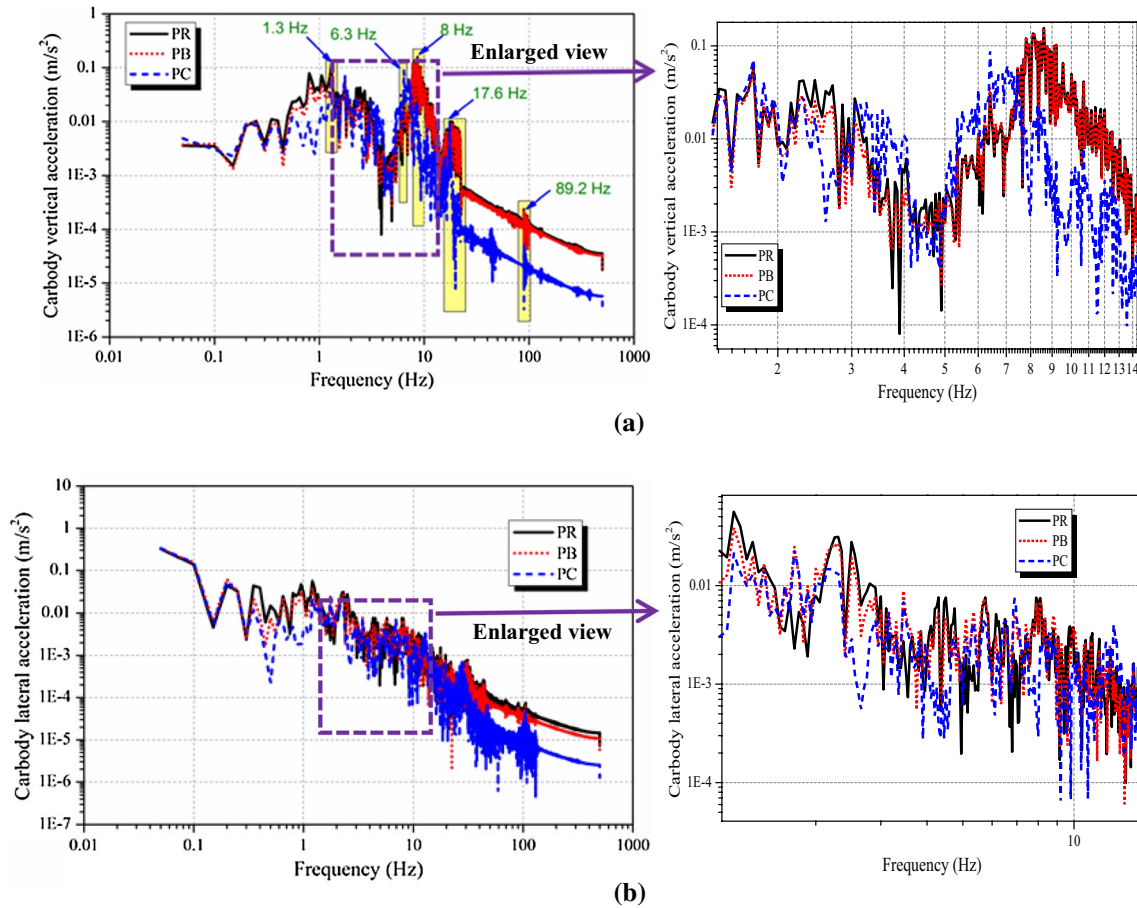
(a)

(b)

Fig. 16 Carbody vertical acceleration on curve segment in frequency domain ($v = 80$ km/h): **a** Vertical acceleration, and **b** Lateral acceleration
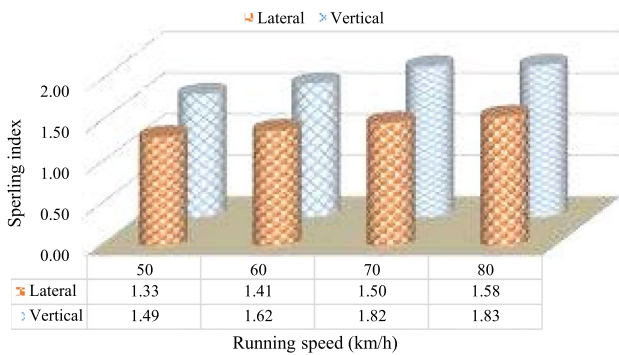

Fig. 17 Sperling index on curve segment

6 Evaluation on ride comfort of metro vehicle subject to short-wave excitation

Corrugation, a kind of short-wave excitation, is commonly occurred in metro line, hence this part evaluates the ride comfort of metro vehicle subject to corrugation excitation.

Because this kind of short-wave excitation has little influence on lateral vibration, the vertical vibration is concerned in this section. Taking the results at 80 km/h for instance, Fig. 18 gives the carbody vertical acceleration at PR location. As seen from the result, the carbody vibrates in response to the corrugation with the same frequency.

The carbody accelerations at different locations at different speeds are shown in Fig. 19. As seen from the result, with the increase of running speed, the accelerations at different location increase. It should be note that, the vertical acceleration at PC location is smallest at 50 km/h, while is largest at 80 km/h, indicating that the acceleration at PC location is most sensitive to running speed subject to the adopted corrugation.

Moreover, the calculated Sperling index subject to corrugation is very small, indicating that the short-wave excitation mainly affects running safety, while has only a little influence on ride comfort of metro train.
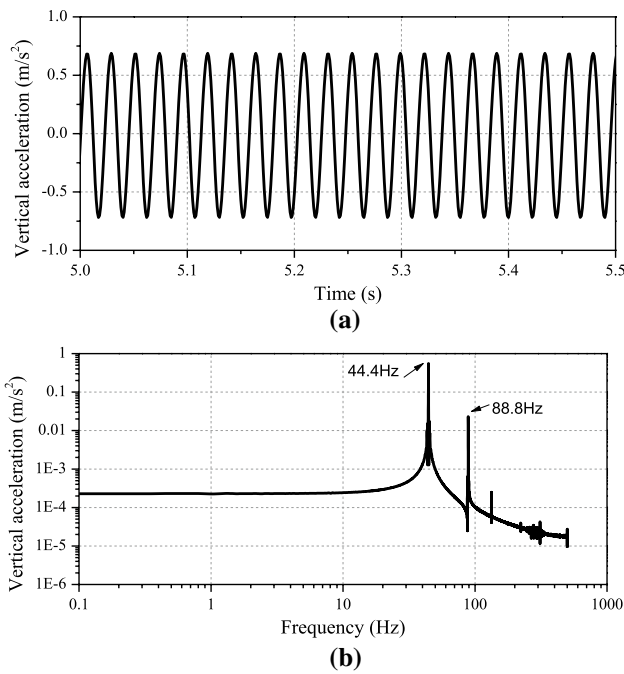
Fig. 18 Carbody vertical acceleration at PR location subject to corrugation (short-wave excitation): **a** in time domain, and **b** in frequency domain
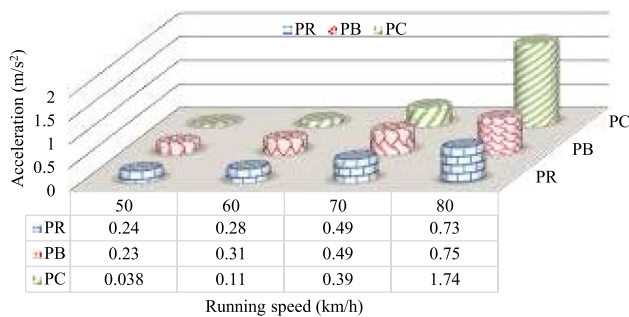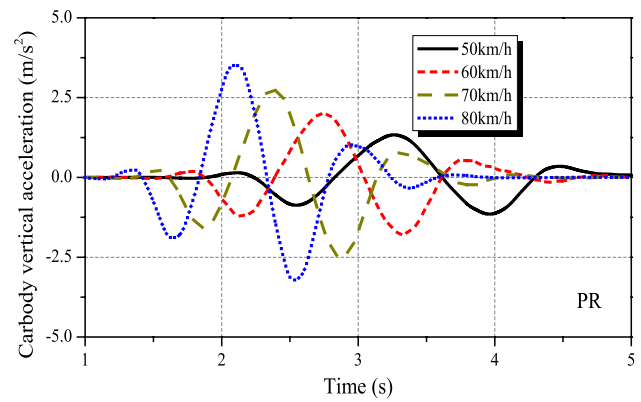

Fig. 19 Carbody accelerations at different locations at different speeds

7 Evaluation on ride comfort of metro vehicle subject to long-wave excitation

To evaluate the ride comfort of metro vehicle subject to long-wave excitation, settlement is chosen in the calculation, and the parameters are given in Sect. 4.

Figure 20 gives the vertical acceleration of carbody at PR location subject to settlement. The settlement excitation has great influence on carbody vertical acceleration. With the increase of running speed, the carbody acceleration increases sharply.

Fig. 20 Carbody vertical acceleration (PR location) subject to settlement
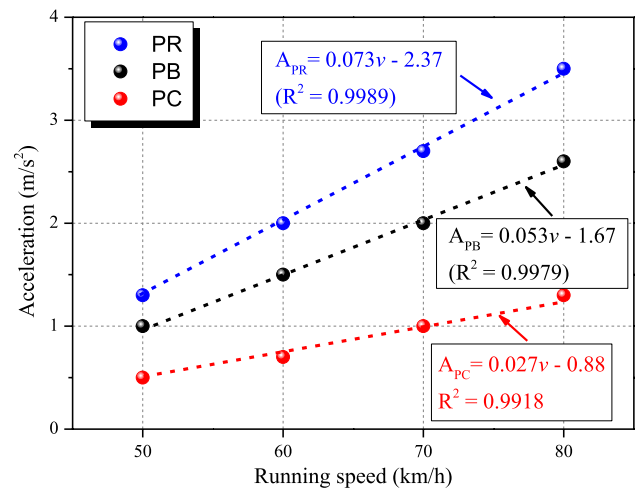
Fig. 21 Peak acceleration values at different speeds

Figure 21 illustrates the peak acceleration values at different speeds. It can be clearly seen from this figure that, carbody acceleration increases linearly with the increase of running speed. All the fitting factors of the fitting expressions are larger than 0.99, indicating a strong linear relationship between running speed and acceleration. The acceleration at PR location is the largest, while that at PC location is the smallest subject to settlement excitation.

Furthermore, the Sperling index subject to settlement is given in Fig. 22. As clearly seen from the results, long-wave excitation has greatly influence on ride comfort of metro train. The Sperling index increases sharply with the increase of running speed subject to settlement excitation.

Among all the evaluation conditions, the long-wave excitation has the greatest influence on ride comfort of metro train, indicating that long-wave excitation in track system should be paid special attention to.
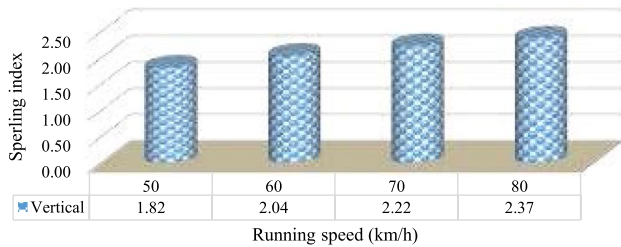
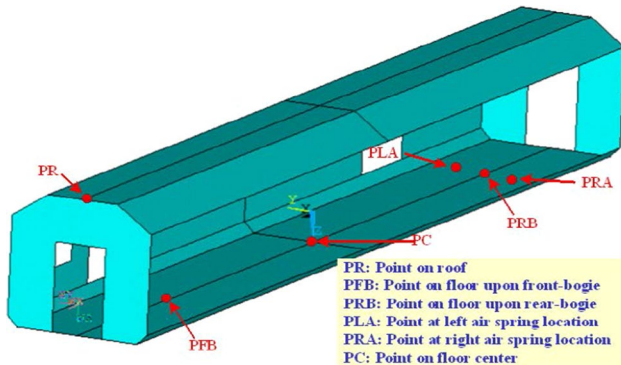**Fig. 22** Sperling index subject to settlement

Fig. 23 Six chosen locations on carbody

8 Deep discussion of carbody vibration at different locations

Carbody vibrations of metro vehicle at three different locations are investigated in the above sections, however, three locations may be not enough to present the whole carbody. Hence, more results are discussed in this section to deeply discuss the carbody vibration.

It should be noted that it is impossible to choose every point on carbody due to huge workload. Hence, in this section, six locations are chosen due to the page limitation, namely PR, PFB, PRB, PLA, PRA and PC (Fig. 23). Additional more results at more locations will be discussed in further works.

Subject to rail random irregularity, vertical and lateral accelerations at these six locations are displayed in Fig. 24.

As seen from the above results:

a. The vibrations at PRB, PLA and PRA locations are almost the same, as well as the peak values, indicating that local vibrations near PRB location are small.

b. Vibration at PC location is the smallest, which is much smaller than vibrations at PRB and PFB locations, indicating that the bending modes and flexible characteristics of carbody have great influences on carbody vibrations.

c. Vibration at PFB location is a little smaller than that at PRB location, which is caused by the movement of running vehicle and the excitation of rail random irregularity.

d. Vibrations at roof do not show great special differences.

e. It is not accurate enough to evaluate ride comfort of metro vehicle only according to vibration at floor center, and more data at different locations should be concerned, especially vibrations at air spring locations.
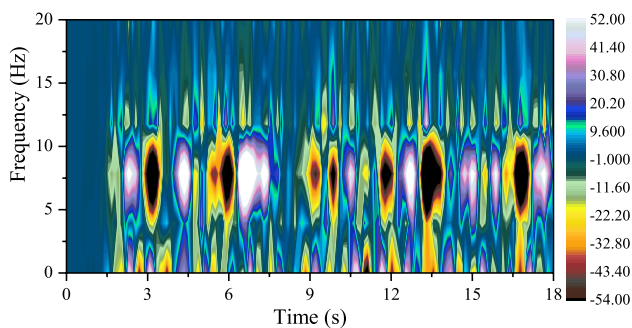
Fig. 24 Carbody vertical acceleration at different locations
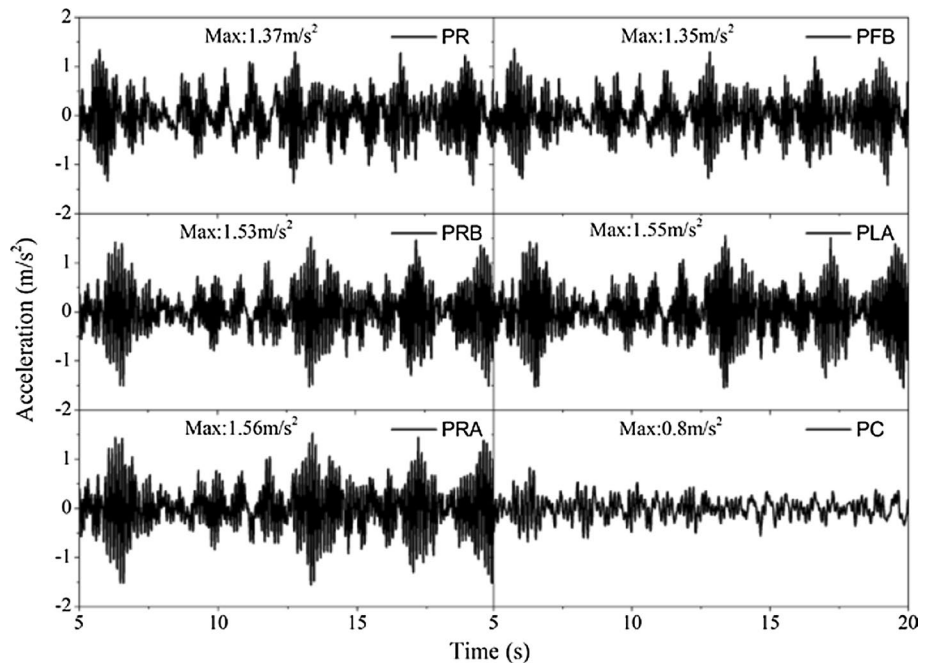
Furthermore, vibration at PRB location in time–frequency domain is given in Fig. 25. As seen from the results, energy of the vertical acceleration is concentrated in the frequency bands of 0–2.5 Hz and 6–9 Hz, which is almost the same as vibrations at other concerned locations. To deeply investigate the relationship among the data of accelerations, correlation analysis is conducted, as seen in Fig. 26.
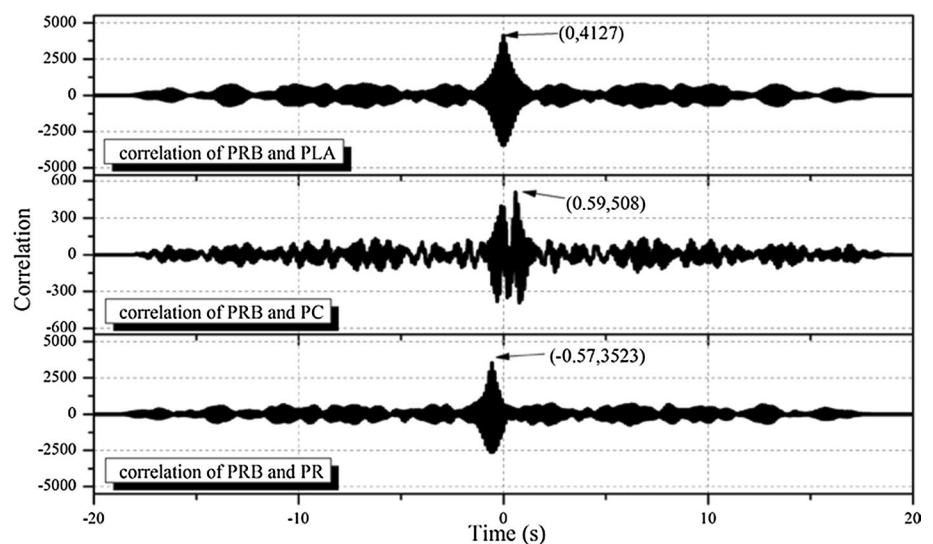
As seen from Fig. 26, the following conclusions can be obtained:

a. Cross-correlations of acceleration (PRB) and acceleration (PLA) is the largest due to the distance of these two location is very short, and local vibrations are not obviously aroused in this area. Moreover, the vibrations at PRB location and PLA location are almost synchronous.
b. Cross-correlations of acceleration (PRB) and acceleration (PC) is the smallest, indicating that bending modes of carbody are greatly excited.
c. Two peaks exist in the correlations of acceleration (PC) and acceleration (PRB). The smaller peak appears at origin of coordinates, while the bigger peak appears at

shifted coordinate, indicating that the vibration at PC location has an inherent relevance with vibrations at PRB location.
d. Maximum value of the cross-correlation of acceleration (PRB) and acceleration (PR) locates at coordinate (− 0.57, 3523), indicating that shift of 0.57 s on timeline exists due to the distance between these two points.

9 Conclusion

This work has presented an evaluation of ride comfort of metro vehicle based on flexible multi-body dynamics, and the ride comfort of metro vehicle on straight line and curve line has been evaluated subjected to rail random irregularity, short-wave excitation and long-wave excitation. Finally, correlations of carbody vibrations at different locations have been deeply investigated. Through the research, the following conclusions are reached.

1. The proposed methodology is effective to evaluate ride comfort of metro vehicle. Ride comfort of metro vehicle can be more accurately evaluated with the flexible vehicle model due to the results obtained by flexible model obviously reflect the sensitive frequency band of human compared to rigid model;
2. Flexible modes and local vibration are obviously reflected in carbody vibrations. Vibration at PR location is largest, while vibration at PC location is smallest.
3. Under different conditions, vertical Sperling indices are almost larger than lateral Sperling indices. With the adopted parameters in this work, the calculated Sperling indices are less than the ruled value in relevant code.
4. Ride comfort is very sensitive to long-wave excitation while is not sensitive to short-wave excitation.

Fig. 25 Vertical accelerations at PRB location in time–frequency domain

Fig. 26 Cross-correlations of carbody accelerations at different locations

5. It is not accurate enough to evaluate ride comfort of metro vehicle only according to vibration at floor center, and more data at different locations should be concerned, especially vibrations at air spring locations.

Due to the page limitation, six locations are chosen in this work, and more locations will be concerned in further investigations to explore the whole carbody vibration considering structural flexibility.

Declarations

Conflict of interest The authors declare no conflict of interest in preparing this article.

References

1. Iwnicki SD. Handbook of railway vehicle dynamics. CRC/Taylor & Francis, 2006.
2. Zhai WM. Vehicle-track coupled dynamics. Beijing: Science press; 2015.
3. Pradhan S, Samantaray AK. Integrated modeling and simulation of vehicle and human multi-body dynamics for comfort assessment in railway vehicles. J Mech Sci Technol. 2018;32(1):109–19.
4. Timoshenko SP, Langer BF. Stresses in railroad track. ASME Trans. 1932;54:2772–93.
5. Escalona JL, Sugiyama H, Shabana AA. Modelling of structural flexiblity in multibody railroad vehicle systems. Veh Syst Dyn. 2013;51(7):1027–58.
6. Shabana AA. Dynamics of multibody systems. 3rd ed. Cambridge: Cambridge University Press; 2005.
7. Sun S, Wang W, Liu J, Li H. Study of carbody's severe vibration based on stability analysis of vehicle system. China Railway Sci. 2012;33(2):82–8.
8. Gerardin M, Cardona A. Flexible multibody dynamics: a finite element approach. Chichester: John Wiley & Sons Publishing House; 2001.
9. Huang CH, Zeng J, Liang SL. Carbody hunting investigation of a high speed passenger car. J Mech Sci Technol. 2013;27(8):2283–92.
10. Shi H, Wu P. Flexible vibration analysis for car body of high-speed EMU. J Mech Sci Technol. 2016;30(1):55–66.
11. Gong D, Zhou J, Sun W. On the resonant vibration of a flexible railway car body and its suppression with a dynamic vibration absorber. J Vib Control. 2012;19(5):649–57.
12. Claus H, Schiehlen W. Modeling and simulation of railway bogie structural vibrations. Veh Syst Dyn. 1998;29:538–52.
13. Claus H, Schiehlen W. Symbolic-numeric analysis of flexible multibody systems. Mech Struct Mach. 2002;30(1):1–30.
14. Carlbom PF. Combining MBS with FEM for rail vehicle dynamics analysis. Multibody Syst Dyn. 2001;6(3):291–300.
15. Saporito G, Baroni A, Romani M. Multi-purpose flexible bodies integration into the multi-body system of a metro-vehicle, ASME 2010 10th Biennial Conference on Engineering Systems Design and Analysis. 2010.
16. Bampton MCC, Craig JRR. Coupling of substructures for dynamic analyses. AIAA J. 1968;6(7):1313–9.
17. Fehr J, Eberhard P. Error-controlled model reduction in flexible multibody dynamics. J Comput Nonlinear Dyn. 2010;5(3):470–8.
18. Yoo WS, Haug EJ. Dynamics of flexible mechanical systems using vibration and static correction modes. J Mech Des. 1986;108(3):315.
19. Wu P, Xue S, Yang C. Dynamics response of high speed passenger car based on flexible car body model. J Traffic Transp Eng. 2005;5:5–8.
20. Zhai WM, Cai CB. Train/track/bridge dynamic interactions: Simulation and applications. Veh Syst Dyn. 2002;37(S):653–65.
21. Zhai W, Xia H, Cai C, et al. High-speed train–track–bridge dynamic interactions–part I: theoretical model and numerical simulation. Int J Rail Transp. 2013;1(1–2):3–24.
22. Ni C, Wang Y. A brief discussion for ride index and comfort. Railway Locomotive & Car. 2003;23(06):1–3.
23. Huang C, Zeng J, Luo R. Vibration suppression of lightweight high speed carbody structure, Proceedings of International Symposium on Dynamics of Vehicles on Roads and Tracks, Manchester, 2011.